

An Eulerian Data Assimilation Method for Two-Layer Quasi-Geostrophic Model in Physical Domain

Hyeonggeun Yun¹ and Quanling Deng^{2,3}

¹School of Computing, Australian National University, Canberra, ACT 2601, Australia (Geun.Yun@anu.edu.au)

²Yau Mathematical Sciences Center, Tsinghua University, Beijing, 100084, China (qldeng@tsinghua.edu.cn)

³School of Computing, Australian National University, Canberra, ACT 2601, Australia (Quanling.Deng@anu.edu.au)

October 20, 2025

Contents

1	Introduction	2
2	Problem statement and numerical schemes	4
2.1	Two-layer Quasi-geostrophic (QG) model	4
2.2	Numerical schemes	5
2.2.1	Temporal discretization	5
2.2.2	Spatial discretization	6
2.2.3	Numerical setup	7
3	Eulerian data assimilation	8
3.1	Conditional Gaussian Nonlinear System (CGNS)	8
3.2	EuDA for recovery of the vorticity	10
3.3	EuDA for recovery of the second layer	12
4	Numerical experiments	18
4.1	EuDA for recovery of the vorticity and the second-layer flow	19
4.2	An application to sea ice floe dynamics with QG ocean flow	22
5	Conclusion	23

Keywords: Data assimilation, quasi-geostrophic model, conditional nonlinear Gaussian system, nonlinear filter

Abstract

Data assimilation (DA) integrates observational data with numerical models to improve the prediction of complex physical systems. However, traditional DA methods often struggle with nonlinear dynamics and multi-scale variability, particularly when implemented directly in the physical domain. To address these challenges, this work develops an Eulerian Data Assimilation (EuDA) framework with the Conditional Gaussian Nonlinear System (CGNS). The proposed approach enables the treatment of non-periodic systems and provides a more intuitive representation of localized and time-dependent phenomena. The work considers a physical domain inspired by sea-ice floe trajectories and ocean eddy recovery in the Arctic regions, where the model dynamics are modeled by a two-layer quasi-geostrophic (QG) system. The QG equations are numerically solved using forward-Euler time stepping and centered finite-difference schemes. CGNS provides a nonlinear filter as it offers an analytical and continuous formulation for filtering a nonlinear system. Model performance is assessed using normalized root mean square error (RMSE) and pattern correlation (Corr) of the posterior mean. The results show that both metrics improve monotonically with increasing timesteps, while RMSE converges to approximately 0.1 across all grid sizes and Corr increases from 0.64 to 0.92 as grid resolution becomes finer. Lastly, a coupled scenario with sea-ice particles advected by the two-layer QG flow under a linear drag force is examined, demonstrating the flexibility of the EuDA–CGNS framework in capturing coupled ice–ocean interactions. These findings demonstrate the effectiveness of exploiting the two-layer QG model in the physical domain to capture multiscale flow features.

1 Introduction

Data assimilation (DA) has become an essential tool for improving predictions of complex physical systems, especially in fields like meteorology, oceanography, and climate science, where observational data are sparse or noisy with high model uncertainties [1, 15]. The purpose of DA is to merge observational data with numerical model predictions to achieve an optimal estimate of the system’s state [15]. By assimilating real-time observations into predictive models, DA can reduce forecast errors and enhance the temporal consistency of simulations.

Traditional DA methods, however, face limitations when applied to systems characterized by multi-scale dynamics and significant nonlinearity. Lagrangian DA, for example, is well-suited to capturing small-scale structures through particle trajectories but is computationally demanding due to high dimensionality and nonlinearity in the Lagrangian observations [11]. On the other hand, Eulerian Data Assimilation (EuDA) provides computational efficiency in representing large-scale flow fields on fixed grids, yet often lacks the resolution needed for smaller-scale features [17]. These challenges are exacerbated in environments with both large-scale and fine-scale structures, such as ocean eddies or atmospheric fronts, where accurate tracking of particle movements is essential for high-fidelity modeling [27]. Out of these two DA methodologies, this work develops an EuDA method formulated directly in the physical domain to recover the physical attributes of the sea ice floe in Arctic regions. This framework enables the model to capture localized, time-dependent phenomena more intuitively compared to other commonly used methods in spectral or Fourier space.

The model is chosen to be based on a two-layer quasi-geostrophic (QG) system for providing a simplified yet physically grounded representation of large-scale geophysical flows. The QG model captures essential

barotropic and baroclinic interactions, and remains a cornerstone in studies of mid-latitude atmospheric and oceanic dynamics [2, 27]. In this context, the Eulerian framework is enhanced through the Conditional Gaussian Nonlinear System (CGNS), which allows continuous and analytically tractable filtering for nonlinear dynamical systems. This is achieved through exploitation of the conditional Gaussian structure, which provides closed-form expressions for conditional mean and covariance, enabling efficient and stable assimilation without ensemble sampling [4].

Hence, the main objective of this study is to evaluate the effectiveness of applying the EuDA framework based on CGNS to the two-layer QG model (see Figure 1). The performance of the assimilated posterior mean is assessed using root mean square error (RMSE) and pattern correlation (Corr), which collectively measure reconstruction accuracy and spatial coherence. The results demonstrate that the EuDA approach can recover physically consistent fields while maintaining computational efficiency.

The rest of the paper is organized as follows. Section 2 presents the formulation of the two-layer QG model and describes the employed numerical schemes in both spatial and temporal dimensions. Section 3 details the proposed EuDA method using CGNS. Section 4 discusses numerical experiments, including simulation results and their evaluation. Finally, Section 5 concludes the paper with remarks and potential future extensions of this work.

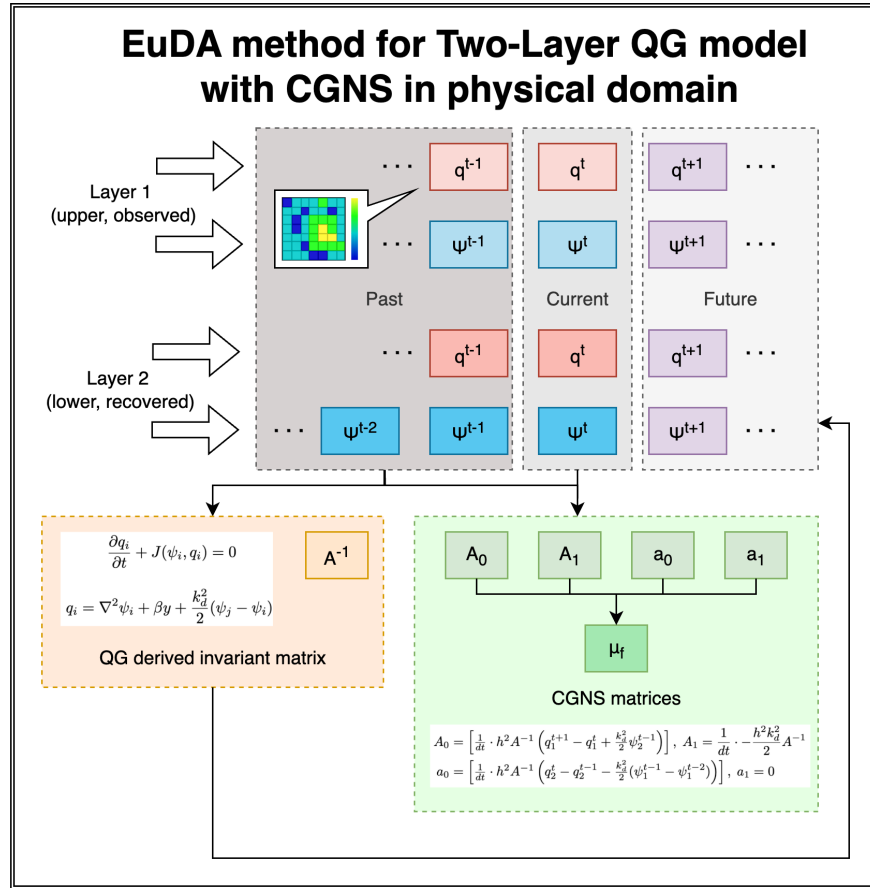


Figure 1: Flowchart of the proposed method

2 Problem statement and numerical schemes

2.1 Two-layer Quasi-geostrophic (QG) model

As the aim of the research focuses on the data assimilation framework for a specific landscape like the Arctic, careful consideration is required in adopting the ocean or atmospheric model. The QG model was deemed to be suitable with the following assumptions. The model is underpinned by a small Rossby number ($R_o \ll 1$) that makes the flow nearly geostrophic, which implies significantly smaller inertia forces than Coriolis forces [32, 9]. The Rossby number is given by

$$R_o = \frac{U}{fL}, \quad (1)$$

where U is a typical horizontal velocity, L is the horizontal length scale, and f is the Coriolis parameter. Such a discrepancy suits a condition with predominantly horizontal flow. Another underlying assumption is the assertion of a hydrostatic balance in vertical motion [32, 9]. This means the vertical pressure gradient is balanced by the gravitational force, effectively allowing the model to ignore vertical accelerations. This is captured by the equation

$$\frac{\partial p}{\partial z} = -\rho g, \quad (2)$$

where p is the pressure, z is the vertical coordinate, ρ is the fluid density and g is the acceleration due to gravity. Furthermore, the flow is assumed to be incompressible in baroclinic models, which means the density does not change significantly with time or space in the horizontal directions [32, 9]. This assumption makes the use of a constant density possible. Altogether, it should be clear that the assumptions resemble large-scale, slow-moving flows in the ocean and atmosphere, such as those found in the Arctic.

The main advantage of the QG model in the given context is its simplicity to work for two layers. This two-layer QG can recover the important physical attributes at one depth, such as streamline function (ψ) and potential vorticity (q), by observing those of other depths. In simplified form, the two-layer QG governing equations are [32, Sect. 5]:

$$\frac{\partial q_i}{\partial t} + J(\psi_i, q_i) = 0 \quad (3)$$

$$q_i = \nabla^2 \psi_i + \beta y + \frac{k_d^2}{2} (\psi_j - \psi_i), \quad (4)$$

where $i = \{1, 2\}$ denotes the level index, $j = 3 - i$ and the Jacobian is $J(\psi_i, q_i) = \frac{\partial \psi}{\partial x} \frac{\partial q}{\partial y} - \frac{\partial \psi}{\partial y} \frac{\partial q}{\partial x}$. For well-posedness, the two-layer QG model is subject to initial and boundary conditions, which will be specified later for the simulations. For the sake of simplicity, the model is assumed to have no external force on the surface and the depths of layers are even. Hence, the assumptions result in 0 for the RHS of Equation (3) and $\frac{k_d^2}{2}$ for Equation (4), respectively. Along with the assumptions, Table 1 illustrates the scale of the model, by providing the typical order of magnitude of relevant parameters. These were then adjusted and scaled accordingly throughout any computation involving the QG model (see Table 3). The Laplacian discretization constant will further be discussed in Section 2.2.2, as it has been manually derived from the discretization process.

Name	Symbol	Typical order of magnitude
Streamline function	ψ	Depends on the initial streamline function
Potential vorticity	q	Depends on the initial streamline function
Coriolis parameter	f_0	$10^{-4} s^{-1}$
Beta parameter	β	$10^{-11} t^{-1} s^{-1}$
Rossby radius of deformation	L_d	$50 \sim 100 km$
Layer thickness	H	$100 \sim 1000 m$
Buoyancy frequency	N	$10^{-2} s^{-1}$
Square of the deformation wavenumber	k_d^2	$10^{-7} m^{-2}$

Table 1: parameters for the two-layer QG model with their typical order of magnitude.

Despite a clear existence of coupling between layers from Equation (4), the decoupling of the two layers for the DA setting is relatively simple as ψ_j only appears once from the perspective of layer i . Another notable insight is the absence of a time-derivative term for ψ_i , insinuating its necessity to couple with q_i to exploit the parameter in a temporal perspective. These relationships provide the dynamical basis for the Eulerian assimilation framework developed in Section 3, where the coupled evolution of ψ and q forms the state equations in the CGNS.

For the DA filtering process, one augments each prognostic PV equation with an additive process-noise term that represents unresolved physics and model error; this noise is taken to be Gaussian white noise and typically spatially correlated through a prescribed covariance (see, e.g., [29]). To keep the numerical scheme presentation straightforward, we omit this stochastic term in the model discretization exposition and introduce it later when applying the DA method as part of the overall modeling and discretization errors in the assimilation setup.

2.2 Numerical schemes

2.2.1 Temporal discretization

Various time-integration schemes have been developed for QG models, including Leapfrog, Runge-Kutta, and semi-implicit formulations [3, 22, 24]. These higher-order approaches often achieve greater accuracy and phase stability for oscillatory flows but introduce additional computational cost and complexity. Given that the primary aim of this study is to establish and evaluate the EuDA framework formulated under the CGNS, the focus is placed on a time-stepping scheme that is explicit, interpretable, and fully compatible with the incremental updates required by CGNS. Accordingly, we use a first-order explicit forward-Euler step for time discretization of the deterministic two-layer QG forecast. When the additive Gaussian white noise is introduced in the data assimilation setting, the natural counterpart is the Euler–Maruyama scheme: it retains the forward-Euler update and augments each step with a mean-zero Gaussian increment whose spatial covariance matches the prescribed model-error covariance and whose magnitude scales with the square root of the time step. This choice delivers first-order accuracy in the weak sense (and one-half order in the strong sense) for the stochastic forcing while keeping the same CFL restriction as the underlying explicit method. In practice, the noise field at each step is generated by sampling i.i.d. standard normals, mapping them through a square root of the spatial covariance, and scaling by the square root of the time step. For clarity of exposition, we present the core scheme with forward Euler and introduce the Euler–Maruyama

augmentation when the DA method is applied.

Let $T > 0$ be the final time and choose an integer $N \geq 1$ as the number of time steps. Define the uniform time step $\Delta t := T/N$ and the grid points $t^n := n \Delta t, n = 0, 1, \dots, N$, so that $0 = t^0 < t^1 < \dots < t^N = T$. The forward-Euler scheme approximates the temporal derivative of a state variable ϕ (e.g., potential vorticity or streamfunction) as

$$\phi^{n+1} = \phi^n + \Delta t f(\phi^n), \quad (5)$$

where $f(\phi^n)$ denotes the governing tendency term evaluated at the current time level and Δt is the time step. Despite being first-order accurate in time, the method is straightforward to implement and ensures a transparent relationship between consecutive states ϕ^n and ϕ^{n+1} , which aligns naturally with the conditional mean and covariance updates in the CGNS formulation. The simplicity of the explicit formulation also facilitates direct control of numerical stability and error propagation, which is advantageous for diagnosing the physical consistency of the assimilation process [20, 14].

To maintain numerical stability, the time step Δt was chosen to satisfy the Courant-Friedrichs-Lewy (CFL) criterion $U_{\max} \frac{\Delta t}{h} \leq 1$, where U_{\max} is the characteristic advective velocity and h is the grid spacing [8]. This constraint ensures numerical stability. In this study, $\Delta t = 10^{-4}$ was found to provide a balance between accuracy and computational efficiency for the QG model.

The forward-Euler integration advances the prognostic variable q_i of each layer according to

$$q_i^{n+1} = q_i^n - \Delta t J(\psi_i^n, q_i^n), \quad (6)$$

where $J(\psi_i, q_i)$ is the Jacobian representing the nonlinear advection of potential vorticity. The resulting updated vorticity field is then inverted to obtain the new streamfunction $\psi_i^{t+\Delta t}$ via the discretized elliptic relation described in the following subsection. This sequential update forms the backbone of the numerical solver that generates the forecast state for the Eulerian assimilation procedure.

In summary, while higher-order schemes could offer enhanced temporal accuracy, the forward-Euler approach was deliberately chosen for its conceptual transparency, analytical compatibility with the CGNS framework, and computational tractability. These attributes make it particularly suitable for validating the underlying physical consistency of the proposed EuDA method.

2.2.2 Spatial discretization

Let the two-layer QG model (3) and (4) be defined on the unit-square domain $\Omega = [0, 1] \times [0, 1]$. Consider a uniform grid of size $N_x \times N_y$ with $h_x := \frac{1}{N_x}, h_y := \frac{1}{N_y}$, and grid nodes $x_i := i h_x$ ($i = 0, \dots, N_x$), $y_j := j h_y$ ($j = 0, \dots, N_y$). For a sufficiently smooth scalar field $u : \bar{\Omega} \rightarrow \mathbb{R}$, denote its grid values by $u_{i,j} \approx u(x_i, y_j)$. Interior indices are $\mathcal{I} = \{1, \dots, N_x - 1\} \times \{1, \dots, N_y - 1\}$. With this setting in mind, the governing equations are rewritten as

$$\frac{\partial q}{\partial t} + \frac{\partial \psi}{\partial x} \frac{\partial q}{\partial y} - \frac{\partial \psi}{\partial y} \frac{\partial q}{\partial x} = 0, \quad (7)$$

$$q_i = \nabla^2 \psi_i + \beta y + \frac{k_d^2}{2} (\psi_j - \psi_i), \quad (8)$$

and they are discretized at each grid cell (x_k, y_l) for layers $i, j \in \{1, 2\}$ using the second-order central finite difference method [27]. Firstly, with the forward Euler scheme for the temporal dimension, the Jacobian

term in Equation (7) is computed as:

$$q_{k,l}^{n+1} - q_{k,l}^n = \left(\frac{\psi_{k,l+1}^n - \psi_{k,l-1}^n}{2h_y} \frac{q_{k+1,l}^n - q_{k-1,l}^n}{2h_x} - \frac{\psi_{k+1,l}^n - \psi_{k-1,l}^n}{2h_x} \frac{q_{k,l+1}^n - q_{k,l-1}^n}{2h_y} \right) \Delta t, \quad (9)$$

where the superscript denotes the time marching. This update is combined with the temporal scheme from Section 2.2 to advance q explicitly at each time step.

The streamfunction ψ_i is obtained by numerically inverting the elliptic relation (8). Rearranging gives

$$\nabla^2 \psi_i - \frac{k_d^2}{2} \psi_i = q_i - \beta y - \frac{k_d^2}{2} \psi_j. \quad (10)$$

Consider a uniform grid case with $h_x = h_y = h$. We apply the same finite-difference scheme to the Laplacian to obtain

$$\frac{\psi_{i_{k+1,l}} + \psi_{i_{k-1,l}} + \psi_{i_{k,l+1}} + \psi_{i_{k,l-1}} - 4\psi_{i_{k,l}}}{h^2} - \frac{k_d^2}{2} \psi_{i_{k,l}} = \hat{F}_{k,l}, \quad (11)$$

with $\hat{F}_{k,l} = q_{i_{k,l}} - \beta y_l - \frac{k_d^2}{2} \psi_{j_{k,l}}$ being the right-hand side. This can be compactly written in matrix form as

$$A\psi = F. \quad (12)$$

For the entries near boundaries, we apply the doubly periodic boundary conditions in both x and y directions:

$$\psi_i(0, y, t) = \psi_i(L_x, y, t), \quad \psi_i(x, 0, t) = \psi_i(x, L_y, t).$$

We remark that alternative spatial discretizations, such as finite element [13, 12] or isogeometric analysis [7, 10], can be adopted when geometric fidelity or unstructured meshes are required. In this work, we use a standard second-order central finite-difference scheme on a uniform grid to keep the implementation simple and to focus on the data assimilation (DA) workflow. For our objectives, higher-order spatial accuracy is not rate-limiting: the dominant errors arise from the DA process and model uncertainty rather than from spatial truncation. The proposed DA framework remains unchanged if a different consistent spatial discretization is employed.

2.2.3 Numerical setup

With the temporal and spatial discretization schemes, the numerical implementation solves for ψ_i and q_i on a two-dimensional, uniform grid as follows. The two governing Equations (7) and (8) are coupled at each time step, where Equation (7) provides the prognostic update for q_i , and Equation (8) yields the diagnostic inversion for ψ_i . These operations define the matrices A_0, A_1, a_0 , and a_1 that later appear in the CGNS filtering stage (Section 3.1).

Analytical integration of these equations is intractable due to the high dimensionality and strong nonlinear coupling between layers [28]. The discretized numerical model therefore, serves as the benchmark generator for testing the CGNS-based assimilation scheme. In this work, a full simulation involves grids up to 50×50 and 2×10^4 time steps. Direct analytical evaluation would require symbolic manipulation of large trigonometric expressions and matrix exponentials, which would take several days in MATLAB, whereas the present finite-

difference solver completes within approximately 30 minutes on a standard workstation.

All simulation parameters are summarized in Tables 2 and 3.

Name	Symbol	Simulation Parameters
Final time	T_f	0.05 ~ 2s
Time-step size	dt	$10^{-4}s$
Mesh grid setting	$N_x \times N_y$	{10 × 10, 30 × 30, 50 × 50}
Initial streamline function 1 (asymmetric sinusoidal)	$\psi_i^{t=0}$	$\psi_1^{t=0}(x, y) = -\sin(1.2\pi x) \sin(1.5\pi y) + 0.6 \cos(2.3\pi x) \cos(2.8\pi y)$
Initial streamline function 2 (symmetric Gaussian)	$\psi_i^{t=0}$	$\psi_2^{t=0}(x, y) = \sin(3.1\pi x) \sin(0.8\pi y) + 0.7 \cos(1.6\pi x) \cos(2.4\pi y)$
Smoothing kernel dimension	$n \times n$	$\psi_1^{t=0}(x, y) = \exp(-(2(x - 1/2)^2 + (y - 1/2)^2)/(2(1/8)^2))$ $\psi_2^{t=0}(x, y) = \exp(-((x - 1/2)^2 + 4(y - 1/2)^2)/(3(1/8)^2))$
		5 × 5

Table 2: Temporal and spatial parameters of the simulation.

Name	Symbol	Parameter Dimensions
Streamfunction	ψ	Depends on initial condition
Potential vorticity	q	Depends on initial condition
Coriolis parameter	f_0	10^{-2} s^{-1}
Beta parameter	β	$10^{-1} \text{ m}^{-1}\text{s}^{-1}$
Rossby radius of deformation	L_d	50 ~ 100 km
Layer thickness	H	100 ~ 1000 m
Buoyancy frequency	N	$10^{-4} \sim 10^{-3} \text{ s}^{-1}$
Square of deformation wavenumber	k_d^2	10 m

Table 3: Physical parameters used for the two-layer QG model.

The spatial domain is square, $(x, y) \in [0, 1] \times [0, 1]$, discretized into $N_x \times N_y$ uniform cells. The time increment $\Delta t = 10^{-4}$ s satisfies the CFL constraint. Two initial conditions are tested: (1) an asymmetric sinusoidal pattern and (2) a symmetric Gaussian field. The former generates complex, chaotic advection patterns representative of realistic mesoscale eddies, and thus is used as a benchmark experiment for the proposed method, while the latter serves as a sanity check for model stability.

For the well-posedness of the two-layer QG model, we impose homogeneous boundary conditions on the streamfunctions. At each time step, q^{n+1} is computed explicitly from q^n and ψ^n using Equation (9), and ψ^{n+1} is recovered by solving the linear system in Equation (12). The overall numerical workflow is summarised in Algorithm 1. Because matrix A remains constant, its decomposition is performed once before the time-marching loop, allowing the update of ψ and q at each iteration to proceed efficiently.

3 Eulerian data assimilation

3.1 Conditional Gaussian Nonlinear System (CGNS)

The CGNS offers a powerful framework to model complex dynamical systems that exhibit both nonlinear and non-Gaussian characteristics [21, 5, 4, 23]. In these systems, while the overall dynamics may be highly nonlinear, the conditional distributions of specific variables retain a Gaussian structure [23, 4]. This property

Algorithm 1 Two-layer QG numerical solver ▷ All computations take place for both layers in parallel

Require: {All the parameters in Tables 2 and 3}
init constants, time variables, and mesh constraints
init compute the invariant matrix \mathbf{A} before time marching
init ψ^1 and q^1 given the initial ψ
for $t = 1 : N_t - 1$ **do**
 compute q^{n+1} by solving Equation (3) with Equation (9)
 compute ψ^{n+1} by solving Equation (4) with Equation (12)
end for
return $\psi^{1:N_t}$ and $q^{1:N_t}$

is especially beneficial for data assimilation, uncertainty quantification, and prediction, as it enables closed-form solutions for conditional mean and covariance, streamlining the analysis and computational tasks associated with high-dimensional, nonlinear systems [33].

The framework typically uses two state variables, \mathbf{X} (observational) and \mathbf{Y} (estimation). It should be noted that each state variable is defined in multi-dimension (i.e. $\mathbf{X} \in \mathbb{C}^{n_1}$ and $\mathbf{Y} \in \mathbb{C}^{n_2}$), as exemplified in Section 3.2. With such state variables, the general form of the CGNS is expressed as:

$$d\mathbf{X} = [\mathbf{A}_0(\mathbf{X}, t) + \mathbf{A}_1(\mathbf{X}, t)\mathbf{Y}] dt + \mathbf{B}_1(\mathbf{X}, t)d\mathbf{W}_1(t), \quad (13)$$

$$d\mathbf{Y} = [\mathbf{a}_0(\mathbf{X}, t) + \mathbf{a}_1(\mathbf{X}, t)\mathbf{Y}] dt + \mathbf{b}_2(\mathbf{X}, t)d\mathbf{W}_2(t), \quad (14)$$

where $\mathbf{A}_0, \mathbf{A}_1, \mathbf{a}_0, \mathbf{a}_1$ denote the system matrices that may vary with both \mathbf{X} and time t , while diffusion matrices \mathbf{B}_1 and \mathbf{b}_2 incorporate stochasticity through independent Wiener processes \mathbf{W}_1 and \mathbf{W}_2 [23, 25]. One beneficial property of the system is its continuity in observing and recovering, unlike traditional data assimilation frameworks, such as the Kalman filter [18, Sect. 21] and Ensemble Kalman filter [30]. This requires more observational data but leads to a smoother propagation of uncertainties over time and, ultimately, more reliable assimilation outcomes compared to other discrete models with an observational interval.

Another key advantage of the CGNS lies in the conditional Gaussian structure, which allows \mathbf{Y} , conditioned on \mathbf{X} , to follow a linear Gaussian process. This relationship simplifies the computation of conditional means (μ_f) and conditional covariances (R_f), which can be derived using the following closed-form expressions [23]:

$$d\mu_f = (a_0 + a_1\mu_f) dt + (R_f A_1^*)(B_1 B_1^*)^{-1} (dX - (A_0 + A_1\mu_f)dt), \quad (15)$$

$$dR_f = [a_1 R_f + R_f a_1^* + b_2 b_2^* - (R_f A_1^*)(B_1 B_1^*)^{-1} (A_1 R_f)] dt, \quad (16)$$

where $*$ is the complex conjugate transpose. This is to be treated as the transpose (n) in the paper, as all values are real numbers. These equations form the basis for optimal filtering within CGNS and enable efficient, scalable computations in high-dimensional systems, such as oceanographic and atmospheric models.

Nevertheless, the most difficult and critical part when implementing the framework involves the derivation of system matrices, especially \mathbf{A}_1 and \mathbf{A}_0 , which are responsible for the coupling between observed and predicted variables. The construction of matrices and their impact on the stability will be among the main discussions of Sections 3.2 and 3.3.

3.2 EuDA for recovery of the vorticity

As a step towards more realistic and complicated cases, the CGNS should first be utilized to recover one of the key state variables of q given its ψ for both layers. Consequently, the observational data and posterior data are defined as below.

$$X = \begin{bmatrix} \psi_1 \\ \psi_2 \end{bmatrix}, Y = \begin{bmatrix} q_1 \\ q_2 \end{bmatrix}. \quad (17)$$

It is worth noting that each state variable is described on 50×50 grid, which each grid can be transformed into this matrix (see Equation (18)):

$$X = \begin{bmatrix} \psi_{1,1,1} & \cdots & \psi_{1,1,50} \\ \vdots & \ddots & \vdots \\ \psi_{1,50,1} & \cdots & \psi_{1,50,50} \\ \psi_{2,1,1} & \cdots & \psi_{2,1,50} \\ \vdots & \ddots & \vdots \\ \psi_{2,50,1} & \cdots & \psi_{2,50,50} \end{bmatrix}, Y = \begin{bmatrix} q_{1,1,1} & \cdots & q_{1,1,50} \\ \vdots & \ddots & \vdots \\ q_{1,50,1} & \cdots & q_{1,50,50} \\ q_{2,1,1} & \cdots & q_{2,1,50} \\ \vdots & \ddots & \vdots \\ q_{2,50,1} & \cdots & q_{2,50,50} \end{bmatrix}. \quad (18)$$

The indexing should not be confused with what has been and will be used throughout the paper, since the above is based on the conventional matrix index, while the custom one resembles Cartesian plane coordinates. In this respect, the operations are mostly done element-wise, except when the entire state has to interact with the other state, namely $A_1 Y$ and $a_1 Y$. This requires careful consideration when decomposing each state variable's time derivative into its constant (A_0 or a_0) and state-dependent ($A_1 Y$ or $a_1 Y$) components. Given this intricacy, it is clearly more ideal to reduce complexity in the matrix multiplication, although some terms are inevitably part of it to capture the stochastic influence of Y .

Similar to the direct numerical solution (see Section 2.2.3), linearizing q (Y) into its matrices is straightforward. Moving the Jacobian term to the other side in Equation (3) yields:

$$dY = dq = -J(\psi, q)dt.$$

Since the Jacobian only consists of terms that are the multiplication of each state variable, there is no independent term from Y . Hence, the entire expression must be captured under $a_1 Y$, despite knowing it is not ideal. In fact, the discretization of the Jacobian term to separate a_1 from $a_1 Y$ is used repeatedly in this CGNS implementation, which is derived as follows. The same indexing scheme as in Equation (9) was used to express the interaction of each cell against every other cell. This results in a_1 with a size of 2500×2500 matrix for a 50×50 mesh.

The discretization uses central finite difference as follows.

$$a_1 \psi = \frac{d\psi}{dy} \frac{dq}{dx} - \frac{d\psi}{dx} \frac{dq}{dy} \quad (19)$$

$$= \frac{\psi_{k,l+1} - \psi_{k,l-1}}{2h_y} \frac{q_{k+1,l} - q_{k-1,l}}{2h_x} - \frac{\psi_{k+1,l} - \psi_{k-1,l}}{2h_x} \frac{q_{k,l+1} - q_{k,l-1}}{2h_y} \quad (20)$$

$$= \frac{(\psi_{k,l+1} - \psi_{k,l-1})(q_{k+1,l} - q_{k-1,l}) - (\psi_{k+1,l} - \psi_{k-1,l})(q_{k,l+1} - q_{k,l-1})}{4h^2} \quad (21)$$

Now consider an n -th cell of a grid, which would be in the n -th row of a_1 when vectorized. The columns in the row will now be

$$\begin{aligned} q_{k+1,l} - q_{k-1,l}, \\ q_{k-1,l} - q_{k+1,l}, \\ q_{k,l-1} - q_{k,l+1}, \\ q_{k,l+1} - q_{k,l-1}, \end{aligned}$$

for positions of $\psi_{k,l+1}, \psi_{k,l-1}, \psi_{k+1,l}, \psi_{k-1,l}$, respectively. As a final note, the matrix should be divided by $4h^2$ element-wise. Such construction of a_1 ensures $a_1\psi = -J(\psi, q)$. Adding white noise terms to the model to include modeling errors for the CGNS DA framework, this results in:

$$dY = \begin{bmatrix} dq_1 \\ dq_2 \end{bmatrix} = \begin{bmatrix} 0 \\ 0 \end{bmatrix} + \begin{bmatrix} -J(\psi_1, q_1) \\ -J(\psi_2, q_2) \end{bmatrix} dt + 0.1\sqrt{dt}\mathcal{N}(0, 1) = [a_0 + a_1Y] dt + b_2(X, t)dW_2(t), \quad (22)$$

where b_2 characterizes the noise strength.

Meanwhile, the decomposition of ψ cannot be as easy as directly using Equation (4) in Section 2.2.3, since CGNS forces both variables to be represented with respect to time to obtain a continuously analytical solution. Hence, Equation (4) must be substituted into Equation (3) as it is the only way to extract a term $\frac{d\psi}{dt}$.

$$\frac{d(\nabla^2\psi_i + \beta y + \frac{k_d^2}{2}(\psi_j - \psi_i))}{dt} = -J(\psi_i, q_i)$$

Note that the values of the y-coordinates y are independent of time, leading to a removal of βy .

$$\frac{d(\nabla^2\psi_i + \frac{k_d^2}{2}(\psi_j - \psi_i))}{dt} = -J(\psi_i, q_i)$$

The issue with the current state of decomposition is that $\frac{d\psi_i}{dt}$ cannot easily be isolated due to the complexity of reversing the $\nabla^2\psi_i$ term. At this point, it was observed that shifting the perspective of j introduces a new paradigm as $\frac{k_d^2}{2}$ was the only variable linked with ψ_j . Hence, swapping the i and j yields

$$\frac{d\psi_j}{dt} = \frac{\partial \left(\psi_i - \frac{2}{k_d^2} \nabla^2 \psi_i \right)}{\partial t} - \frac{2}{k_d^2} J(\psi_i, q_i) \quad (23)$$

Thus, the first term is independent of q , and thus, can be represented as A_0 . This is one novelty of the proposed method for the DA setting. Now, all the system matrices required by the CGNS framework are

obtained, as represented below.

$$dX = \begin{bmatrix} d\psi_1 \\ d\psi_2 \end{bmatrix} = \begin{bmatrix} \frac{\partial \left(\psi_2 - \frac{2}{k_d^2} \nabla^2 \psi_2 \right)}{\partial t} \\ \frac{\partial \left(\psi_1 - \frac{2}{k_d^2} \nabla^2 \psi_1 \right)}{\partial t} \end{bmatrix} + \begin{bmatrix} -\frac{2}{k_d^2} J(\psi_2, q_2) \\ -\frac{2}{k_d^2} J(\psi_1, q_1) \end{bmatrix} dt + \sqrt{5} \sqrt{dt} \mathcal{N}(0, 1) = [A_0 + A_1 Y] dt + B_1(X, t) dW_1(t), \quad (24)$$

$$dY = \begin{bmatrix} dq_1 \\ dq_2 \end{bmatrix} = \begin{bmatrix} 0 \\ 0 \end{bmatrix} + \begin{bmatrix} -J(\psi_1, q_1) \\ -J(\psi_2, q_2) \end{bmatrix} dt + 0.1 \sqrt{dt} \mathcal{N}(0, 1) = [a_0 + a_1 Y] dt + b_2(X, t) dW_2(t), \quad (25)$$

$$A_0 = \begin{bmatrix} \frac{\partial \left(\psi_2 - \frac{2}{k_d^2} \nabla^2 \psi_2 \right)}{\partial t} \\ \frac{\partial \left(\psi_1 - \frac{2}{k_d^2} \nabla^2 \psi_1 \right)}{\partial t} \end{bmatrix}, \quad A_1 = a_1 \begin{bmatrix} 0 & \frac{2}{k_d^2} \\ \frac{2}{k_d^2} & 0 \end{bmatrix} \quad (26)$$

$$a_0 = \begin{bmatrix} 0 \\ 0 \end{bmatrix}, \quad a_1 Y = \begin{bmatrix} -J(\psi_1, q_1) \\ -J(\psi_2, q_2) \end{bmatrix}, \quad (27)$$

where B_1, b_2 are the noise terms. In the numerical experiments, for the diffusion matrices, $B_1 = \sqrt{5}$ and $b_2 = 0.1$ were chosen as default values with conventional Wiener processes being $W_1, W_2 = \mathbf{Rand}(0, 1) \sqrt{dt}$ for each cell of both layers [19] (similar in Section 3.3). The last component to implement was the conditional covariance matrix R_f :

$$C_{Y|X} = \Sigma_{YY} - \Sigma_{YX} \Sigma_{XX}^{-1} \Sigma_{XY}.$$

Since there was no known covariance for the arbitrarily created initial streamline functions, 1% of the simulation time was dedicated to computing a covariance as well as values of both state variables via the numerical solution to reflect the trend truly. It is worth noting that such a technique is widely used at the initial stage of data assimilation to ensure stability [16]. The Algorithm 2 below demonstrates this entire process.

3.3 EuDA for recovery of the second layer

Now that the use of CGNS to recover physical properties of a two-layer QG model is found to be feasible, its applicability in a more realistic setting must be discussed. Hence, this section considers ψ_1 as the only observation, aiming to recover the attributes of the second layer. Since the vorticity among the same layer can be numerically solved as discussed in Section 2.2.3, we set Y as ψ_2 :

$$X = [\psi_1], Y = [\psi_2]. \quad (28)$$

Algorithm 2 Two-layer QG CGNS solver ▷ All computations take place for both layers in parallel

Require: {All the parameters in Tables 2 and 3}

init constants, time variables, and mesh constraints

init compute the invariant matrix A before time marching

init ψ^1, q^1 and μ_f for both layers given the initial ψ

for $t = 1 : \frac{N_t}{100} - 1$ **do**

compute q^{n+1} by solving Equation (3) with (9)

compute ψ^{n+1} by solving Equation (4) with (12)

update $\Sigma\psi$ and Σq for R_f

end for

init R_f based on $\psi^{1:\frac{N_t}{100}}, \Sigma\psi, q^{1:\frac{N_t}{100}}$ and Σq

for $t = \frac{N_t}{100} : N_t$ **do**

compute observational noise

compute ψ^{n+1} with μ_f^n

find A_0, A_1, a_0 and a_1 with Equations (26) and (27)

compute μ_f^{n+1} via CGNS framework with Equation (15)

compute R_f^{n+1} via CGNS framework with Equation (16)

end for

return $\psi^{1:N_t}$ and $\mu_f^{1:N_t}$

Similar to Section 3.2, we set the system as follows.

$$dX = [d\psi_1] = \left[\left[\frac{\partial \left(\psi_2 - \frac{2}{k_d^2} \nabla^2 \psi_2 \right)}{\partial t} \right] + \left[-\frac{2}{k_d^2} J(\psi_2, q_2) \right] \right] dt + \sqrt{5} \sqrt{dt} \mathcal{N}(0, 1) = [A_0 + A_1 Y] dt + B_1(X, t) dW_1(t) \quad (29)$$

$$dY = [d\psi_2] = \left[\left[\frac{\partial \left(\psi_1 - \frac{2}{k_d^2} \nabla^2 \psi_1 \right)}{\partial t} \right] + \left[-\frac{2}{k_d^2} J(\psi_1, q_1) \right] \right] dt + 0.1 \sqrt{dt} \mathcal{N}(0, 1) = [a_0 + a_1 Y] dt + b_2(X, t) dW_2(t) \quad (30)$$

$$A_0 = \left[\frac{\partial \left(\psi_2 - \frac{2}{k_d^2} \nabla^2 \psi_2 \right)}{\partial t} \right], \quad A_1 \psi_2 = -\frac{2}{k_d^2} J(\psi_2, q_2) \quad (31)$$

$$a_0 = \left[\frac{\partial \left(\psi_1 - \frac{2}{k_d^2} \nabla^2 \psi_1 \right)}{\partial t} \right], \quad a_1 \psi_2 = -\frac{2}{k_d^2} J(\psi_1, q_1) \quad (32)$$

However, this derivation was found to be inappropriate in capturing the weak coupling between the two layers. More specifically, it lacks stability when properly discretized, which the form appears to be extremely convoluted, suggesting the disparity between theory and practicality once again. The following derivation demonstrates the infeasibility.

For the sake of readability, let $u = (i, j+1), d = (i, j-1), r = (i+1, j), l = (i-1, j)$ denote the coordinates above, below, to the right, and to the left of a current coordinate (i, j) , respectively. With the established

assumption of equal spacing in x and y dimensions, where $h = dx = dy$,

$$\begin{aligned}
J(\psi_2, q_2) &= \frac{\partial \psi_2}{\partial x} \frac{\partial q_2}{y} - \frac{\partial \psi_2}{\partial y} \frac{\partial q_2}{\partial x} \\
&= \frac{\psi_{2_r} - \psi_{2_l}}{2dx} \frac{q_{2_u} - q_{2_d}}{2dy} - \frac{\psi_{2_u} - \psi_{2_d}}{2dy} \frac{q_{2_r} - q_{2_l}}{2dx} \\
&= \frac{1}{4h^2} ((q_{2_u} - q_{2_d})\psi_{2_r} + (q_{2_d} - q_{2_u})\psi_{2_l} + (q_{2_l} - q_{2_r})\psi_{2_u} + (q_{2_r} - q_{2_l})\psi_{2_d}).
\end{aligned}$$

This discretization computes A_1 . However, a careful approach must be taken for a_1 since the vector ψ_2 does not directly appear on the RHS of the Jacobian with ψ_1 and q_1 .

Hence, Equation (4) was rearranged in terms of ψ_2 and substituted for $a_1\psi_2 = -\frac{2}{k_d^2}J(\psi_1, q_1)$:

$$\begin{aligned}
q_2 &= \nabla^2 \psi_2 + \beta y + \frac{k_d^2}{2}(\psi_1 - \psi_2), \\
\psi_1 &= \frac{2}{k_d^2}(q_2 - \nabla^2 \psi_2 - \beta y) + \psi_2.
\end{aligned}$$

More coordinates notations are used, where $uu, ur, ul, dr, dl, dd, rr, ll$ represents $(i, j + 2), (i + 1, j + 1), (i - 1, j + 1), (i + 1, j - 1), (i - 1, j - 1), (i, j - 2), (i + 2, j), (i - 2, j)$ given a current coordinate of (i, j) .

$$\begin{aligned}
J(\psi_1, q_1) &= J\left(\frac{2}{k_d^2}(q_2 - \nabla^2 \psi_2 - \beta y) + \psi_2, q_1\right) \\
&= \frac{\partial\left(\frac{2}{k_d^2}(q_2 - \nabla^2 \psi_2 - \beta y) + \psi_2\right)}{\partial x} \frac{\partial q_1}{\partial y} - \frac{\partial\left(\frac{2}{k_d^2}(q_2 - \nabla^2 \psi_2 - \beta y) + \psi_2\right)}{\partial y} \frac{\partial q_1}{\partial x}
\end{aligned}$$

discretizes the first term and generalizes it to the second term:

$$\begin{aligned}
&\frac{\partial\left(\frac{2}{k_d^2}(q_2 - \nabla^2 \psi_2 - \beta y) + \psi_2\right)}{\partial x} \frac{\partial q_1}{\partial y} \\
&= \frac{\frac{2}{k_d^2}(q_{2_r} - q_{2_l} - (\nabla^2 \psi_{2_r} - \nabla^2 \psi_{2_l})) + \psi_{2_r} - \psi_{2_l}}{2dx} \frac{q_{1_u} - q_{1_d}}{2dy} \\
&= \frac{\frac{2}{k_d^2}\left(q_{2_r} - q_{2_l} - \left(\frac{\psi_{2_{ur}} + \psi_{2_{dr}} + \psi_{2_{rr}} + \psi_{2_{(i,j)}} - 4\psi_{2_r}}{h^2} - \frac{\psi_{2_{ul}} + \psi_{2_{dl}} + \psi_{2_{(i,j)}} + \psi_{2_{ll}} - 4\psi_{2_l}}{h^2}\right)\right) + \psi_{2_r} - \psi_{2_l}}{2dx} \frac{q_{1_u} - q_{1_d}}{2dy} \\
&= \frac{\frac{2}{k_d^2}\left(q_{2_r} - q_{2_l} - \left(\frac{\psi_{2_{ur}} + \psi_{2_{dr}} + \psi_{2_{rr}} - 4\psi_{2_r} - \psi_{2_{ul}} - \psi_{2_{dl}} - \psi_{2_{ll}} + 4\psi_{2_l}}{h^2}\right)\right) + \psi_{2_r} - \psi_{2_l}}{2dx} \frac{q_{1_u} - q_{1_d}}{2dy} \\
&= \left(\frac{\frac{2}{k_d^2}(q_{2_r} - q_{2_l})}{2dx} - \frac{\frac{2}{k_d^2 h^2}(\psi_{2_{ur}} + \psi_{2_{dr}} + \psi_{2_{rr}} - 4\psi_{2_r} - \psi_{2_{ul}} - \psi_{2_{dl}} - \psi_{2_{ll}} + 4\psi_{2_l}) + \psi_{2_r} - \psi_{2_l}}{2dx}\right) \frac{q_{1_u} - q_{1_d}}{2dy} \\
&= \frac{\frac{2}{k_d^2}(q_{2_r} - q_{2_l})(q_{1_u} - q_{1_d})}{4h^2} - \\
&\frac{2(q_{1_u} - q_{1_d})}{4k_d^2 h^4} \left(\psi_{2_{ur}} + \psi_{2_{dr}} + \psi_{2_{rr}} + \left(\frac{k_d^2 h^2}{2} - 4\right)\psi_{2_r} - \psi_{2_{ul}} - \psi_{2_{dl}} - \psi_{2_{ll}} + \left(\left(4 - \frac{k_d^2 h^2}{2}\right)\psi_{2_l}\right)\right).
\end{aligned}$$

The second term can be computed as follows.

$$\begin{aligned}
& \frac{\partial \left(\frac{2}{k_d^2} (q_2 - \nabla^2 \psi_2 - \beta y) + \psi_2 \right)}{\partial y} \frac{\partial q_1}{\partial x} \\
&= \frac{\frac{2}{k_d^2} (q_{2_u} - q_{2_d} - (\nabla^2 \psi_{2_u} - \nabla^2 \psi_{2_d}) - 2\beta dy) + \psi_{2_u} - \psi_{2_d}}{2dy} \frac{q_{1_r} - q_{1_l}}{2dx} \\
&= \frac{\frac{2}{k_d^2} \left(q_{2_u} - q_{2_d} - \left(\frac{\psi_{2_{uu}} + \psi_{2_{(i,j)}} + \psi_{2_{ur}} + \psi_{2_{ul}} - 4\psi_{2_u}}{h^2} - \frac{\psi_{2_{(i,j)}} + \psi_{2_{dd}} + \psi_{2_{dr}} + \psi_{2_{dl}} - 4\psi_{2_d}}{h^2} \right) - 2\beta dy \right) + \psi_{2_u} - \psi_{2_d}}{2dy} \frac{q_{1_r} - q_{1_l}}{2dx} \\
&= \frac{\frac{2}{k_d^2} \left(q_{2_u} - q_{2_d} - \left(\frac{\psi_{2_{uu}} + \psi_{2_{ur}} + \psi_{2_{ul}} - 4\psi_{2_u} - \psi_{2_{dd}} - \psi_{2_{dr}} - \psi_{2_{dl}} + 4\psi_{2_d}}{h^2} \right) - 2\beta dy \right) + \psi_{2_u} - \psi_{2_d}}{2dy} \frac{q_{1_r} - q_{1_l}}{2dx} \\
&= \left(\frac{\frac{2}{k_d^2} (q_{2_u} - q_{2_d} - 2\beta dy)}{2dy} - \frac{\frac{2}{k_d^2 h^2} (\psi_{2_{uu}} + \psi_{2_{ur}} + \psi_{2_{ul}} - 4\psi_{2_u} - \psi_{2_{dd}} - \psi_{2_{dr}} - \psi_{2_{dl}} + 4\psi_{2_d} h^2) + \psi_{2_u} - \psi_{2_d}}{2dy} \right) \frac{q_{1_r} - q_{1_l}}{2dx} \\
&= \frac{\frac{2}{k_d^2} (q_{2_u} - q_{2_d} - 2\beta h)(q_{1_r} - q_{1_l})}{4h^2} - \\
& \frac{(q_{1_r} - q_{1_l}) \frac{2}{k_d^2 h^2} \left(\psi_{2_{uu}} + \psi_{2_{ur}} + \psi_{2_{ul}} + \left(\left(\frac{k_d^2 h^2}{2} - 4 \right) \psi_{2_u} - \psi_{2_{dd}} - \psi_{2_{dr}} - \psi_{2_{dl}} + \left(\left(4 - \frac{k_d^2 h^2}{2} \right) \psi_{2_d} \right) \right)}{4h^2}}{4h^2} \\
&= \frac{\frac{2}{k_d^2} (q_{2_u} - q_{2_d} - 2\beta h)(q_{1_r} - q_{1_l})}{4h^2} - \\
& \frac{2(q_{1_r} - q_{1_l})}{4k_d^2 h^4} \left(\psi_{2_{uu}} + \psi_{2_{ur}} + \psi_{2_{ul}} + \left(\left(\frac{k_d^2 h^2}{2} - 4 \right) \psi_{2_u} - \psi_{2_{dd}} - \psi_{2_{dr}} - \psi_{2_{dl}} + \left(\left(4 - \frac{k_d^2 h^2}{2} \right) \psi_{2_d} \right) \right) \right).
\end{aligned}$$

This finally produces the entire Jacobian term:

$$\begin{aligned}
J(\psi_1, q_1) &= \frac{\partial \left(\frac{2}{k_d^2} (q_2 - \nabla^2 \psi_2 - \beta y) + \psi_2 \right)}{\partial x} \frac{\partial q_1}{\partial y} - \frac{\partial \left(\frac{2}{k_d^2} (q_2 - \nabla^2 \psi_2 - \beta y) + \psi_2 \right)}{\partial y} \frac{\partial q_1}{\partial x} \\
&= \frac{\frac{2}{k_d^2} (q_{2_r} - q_{2_l})(q_{1_u} - q_{1_d})}{4h^2} - \frac{\frac{2}{k_d^2} (q_{2_u} - q_{2_d} - 2\beta h)(q_{1_r} - q_{1_l})}{4h^2} - \\
& \frac{2(q_{1_u} - q_{1_d})}{4k_d^2 h^4} \left(\psi_{2_{ur}} + \psi_{2_{dr}} + \psi_{2_{rr}} + \left(\left(\frac{k_d^2 h^2}{2} - 4 \right) \psi_{2_r} - \psi_{2_{ul}} - \psi_{2_{dl}} - \psi_{2_{ll}} + \left(\left(4 - \frac{k_d^2 h^2}{2} \right) \psi_{2_l} \right) \right) \right) + \\
& \frac{2(q_{1_r} - q_{1_l})}{4k_d^2 h^4} \left(\psi_{2_{uu}} + \psi_{2_{ur}} + \psi_{2_{ul}} + \left(\left(\frac{k_d^2 h^2}{2} - 4 \right) \psi_{2_u} - \psi_{2_{dd}} - \psi_{2_{dr}} - \psi_{2_{dl}} + \left(\left(4 - \frac{k_d^2 h^2}{2} \right) \psi_{2_d} \right) \right) \right) \\
&= \frac{1}{2k_d^2 h^2} \left[(q_{2_r} - q_{2_l})(q_{1_u} - q_{1_d}) - (q_{2_u} - q_{2_d} - 2\beta h)(q_{1_r} - q_{1_l}) - \right. \\
& \frac{(q_{1_u} - q_{1_d})}{h^2} \left(\psi_{2_{ur}} + \psi_{2_{dr}} + \psi_{2_{rr}} + \left(\left(\frac{k_d^2 h^2}{2} - 4 \right) \psi_{2_r} - \psi_{2_{ul}} - \psi_{2_{dl}} - \psi_{2_{ll}} + \left(\left(4 - \frac{k_d^2 h^2}{2} \right) \psi_{2_l} \right) \right) \right) + \\
& \left. \frac{(q_{1_r} - q_{1_l})}{h^2} \left(\psi_{2_{uu}} + \psi_{2_{ur}} + \psi_{2_{ul}} + \left(\left(\frac{k_d^2 h^2}{2} - 4 \right) \psi_{2_u} - \psi_{2_{dd}} - \psi_{2_{dr}} - \psi_{2_{dl}} + \left(\left(4 - \frac{k_d^2 h^2}{2} \right) \psi_{2_d} \right) \right) \right) \right].
\end{aligned}$$

Similarly, the working below discretizes by replacing q_1 of the Jacobian with its corresponding equation:

$$\begin{aligned} J(\psi_1, q_1) &= J\left(\psi_1, \nabla^2\psi_1 + \beta y + \frac{k_d^2}{2}(\psi_2 - \psi_1)\right) \\ &= \frac{\partial\psi_1}{\partial x} \frac{\partial\left(\nabla^2\psi_1 + \beta y + \frac{k_d^2}{2}(\psi_2 - \psi_1)\right)}{\partial y} - \frac{\partial\psi_1}{\partial y} \frac{\partial\left(\nabla^2\psi_1 + \beta y + \frac{k_d^2}{2}(\psi_2 - \psi_1)\right)}{\partial x}. \end{aligned}$$

The first term is

$$\begin{aligned} &\frac{\partial\psi_1}{\partial x} \frac{\partial\left(\nabla^2\psi_1 + \beta y + \frac{k_d^2}{2}(\psi_2 - \psi_1)\right)}{\partial y} \\ &= \frac{\psi_{1r} - \psi_{1l}}{2dx} \frac{\psi_{1uu} + \psi_{1ur} + \psi_{1ul} - 4\psi_{1u} - \psi_{1dd} - \psi_{1dr} - \psi_{1dl} + 4\psi_{1d} + 2\beta dy + \frac{k_d^2}{2}(\psi_{2u} - \psi_{2d} - \psi_{1u} + \psi_{1d})}{2dy} \\ &= \frac{\psi_{1r} - \psi_{1l}}{2dx} \frac{\psi_{1uu} + \psi_{1ur} + \psi_{1ul} - 4\psi_{1u} - \psi_{1dd} - \psi_{1dr} - \psi_{1dl} + 4\psi_{1d} + 2\beta dy + \frac{k_d^2}{2}(-\psi_{1u} + \psi_{1d})}{2dy} + \\ &\frac{k_d^2(\psi_{1r} - \psi_{1l})}{8dxdy}(\psi_{2u} - \psi_{2d}). \end{aligned}$$

The second term is

$$\begin{aligned} &\frac{\partial\psi_1}{\partial y} \frac{\partial\left(\nabla^2\psi_1 + \beta y + \frac{k_d^2}{2}(\psi_2 - \psi_1)\right)}{\partial x} \\ &= \frac{\psi_{1u} - \psi_{1d}}{2dy} \frac{\psi_{1ur} + \psi_{1dr} + \psi_{1rr} - 4\psi_{1r} - \psi_{1ul} - \psi_{1dl} - \psi_{1ll} + 4\psi_{1l} + \frac{k_d^2}{2}(\psi_{2r} - \psi_{2l} - \psi_{1r} + \psi_{1l})}{2dx} \\ &= \frac{\psi_{1u} - \psi_{1d}}{2dy} \frac{\psi_{1ur} + \psi_{1dr} + \psi_{1rr} - 4\psi_{1r} - \psi_{1ul} - \psi_{1dl} - \psi_{1ll} + 4\psi_{1l} + \frac{k_d^2}{2}(-\psi_{1r} + \psi_{1l})}{2dx} + \\ &\frac{k_d^2(\psi_{1u} - \psi_{1d})}{8dxdy}(\psi_{2r} - \psi_{2l}). \end{aligned}$$

Finally, the Jacobian term is

$$\begin{aligned} J(\psi_1, q_1) &= \frac{\partial\psi_1}{\partial x} \frac{\partial\left(\nabla^2\psi_1 + \beta y + \frac{k_d^2}{2}(\psi_2 - \psi_1)\right)}{\partial y} - \frac{\partial\psi_1}{\partial y} \frac{\partial\left(\nabla^2\psi_1 + \beta y + \frac{k_d^2}{2}(\psi_2 - \psi_1)\right)}{\partial x} \\ &= \frac{\psi_{1r} - \psi_{1l}}{2dx} \frac{\psi_{1uu} + \psi_{1ur} + \psi_{1ul} - 4\psi_{1u} - \psi_{1dd} - \psi_{1dr} - \psi_{1dl} + 4\psi_{1d} + 2\beta dy + \frac{k_d^2}{2}(-\psi_{1u} + \psi_{1d})}{2dy} - \\ &\frac{\psi_{1u} - \psi_{1d}}{2dy} \frac{\psi_{1ur} + \psi_{1dr} + \psi_{1rr} - 4\psi_{1r} - \psi_{1ul} - \psi_{1dl} - \psi_{1ll} + 4\psi_{1l} + \frac{k_d^2}{2}(-\psi_{1r} + \psi_{1l})}{2dx} + \\ &\frac{k_d^2(\psi_{1r} - \psi_{1l})}{8dxdy}(\psi_{2u} - \psi_{2d}) - \frac{k_d^2(\psi_{1u} - \psi_{1d})}{8dxdy}(\psi_{2r} - \psi_{2l}). \end{aligned}$$

For both approaches, the constant term was taken out to be a part of the corresponding A_0 or a_0 as they were independent of $Y = \psi_2$.

As expected, the simulation eventually diverged, though the divergence occurred later for longer time integrations. Since this behavior was inherently dictated by the governing physical equations, it became

necessary to adopt a different perspective that no longer relied directly on Equations (3) and (4).

This leads to the development of an alternative approach that was to exploit the numerical scheme as described in Section 2, because of its well-defined discretization from the analytical solution of the equations. This does not necessarily mean the compromise of accuracy to enhance stability, because the central finite difference will still generate approximations with an error term proportional to h^2 from the discretized form, which happens to take an identical value of h .

As stated in Section 2.2.2, ψ is updated via Equation (12),

$$\begin{aligned}\psi_{i_{k+1},l} + \psi_{i_{k-1},l} + \psi_{i_{k,l+1}} + \psi_{i_{k,l-1}} + D\psi_{i_{k,l}} &= h^2 C_{k,l} = F_{k,l} \\ A\psi &= F,\end{aligned}$$

where $D = -(4 + \frac{h^2 k_d^2}{2})I$ where I is an identity matrix, $F_{k,l} = q_{i_{k,l}} - \beta Y - \frac{k_d^2}{2}\psi_{j_{k,l}}$. From this, the relevant matrices for the CGNS can be constructed as follows.

Let $d\psi_1 = \psi_1^{n+1} - \psi_1^n$ at time t . Then, terms of ψ_1 at each timestep can be expressed as

$$\psi_1^{n+1} = A^{-1}h^2 F \quad (33)$$

$$= h^2 A^{-1} \left(q_1^{n+1} - \beta Y - \frac{k_d^2}{2}\psi_2^n \right), \quad (34)$$

$$\psi_1^n = A^{-1}h^2 F \quad (35)$$

$$= h^2 A^{-1} \left(q_1^n - \beta Y - \frac{k_d^2}{2}\psi_2^{t-1} \right). \quad (36)$$

Substitute them into $d\psi = \psi^{n+1} - \psi^n$:

$$d\psi_1 = h^2 A^{-1} \left(q_1^{n+1} - \beta Y - \frac{k_d^2}{2}\psi_2^n \right) - h^2 A^{-1} \left(q_1^n - \beta Y - \frac{k_d^2}{2}\psi_2^{t-1} \right) \quad (37)$$

$$= h^2 A^{-1} \left(q_1^{n+1} - q_1^n - \frac{k_d^2}{2}(\psi_2^n - \psi_2^{t-1}) \right). \quad (38)$$

This now captures the dynamics of ψ_1 . For ψ_2 , it was necessary to make $d\psi_2 = \psi_2^n - \psi_2^{t-1}$, because q_2^{n+1} is required to be able to use ψ_2^{n+1} , which is not computed at the start. Decrementing a timestep by one also intuitively makes sense since usability of q_2^{n+1} is based on the assumption that ψ_2^{n+1} is found, but the goal of this CGNS is to recover ψ_2^{n+1} .

$$d\psi_2 = h^2 A^{-1} \left(q_2^n - \beta Y - \frac{k_d^2}{2}\psi_1^{t-1} \right) - h^2 A^{-1} \left(q_2^{t-1} - \beta Y - \frac{k_d^2}{2}\psi_1^{t-2} \right) \quad (39)$$

$$= h^2 A^{-1} \left(q_2^n - q_2^{t-1} - \frac{k_d^2}{2}(\psi_1^{t-1} - \psi_1^{t-2}) \right) \quad (40)$$

Using the above definitions of $d\psi_1$ and $d\psi_2$, the system matrices can be computed as follows:

$$dX = [d\psi_1] = \left[\left[\frac{1}{dt} \cdot h^2 A^{-1} \left(q_1^{n+1} - q_1^n + \frac{k_d^2}{2} \psi_2^{t-1} \right) \right] + \left[\frac{1}{dt} \cdot -\frac{h^2 k_d^2}{2} A^{-1} \psi_2^n \right] \right] dt + \sqrt{5} \sqrt{dt} \mathcal{N}(0, 1) \quad (41)$$

$$= [A_0 + A_1 Y] dt + B_1(X, t) dW_1(t), \quad (42)$$

$$dY = [d\psi_2] = \left[\frac{1}{dt} \cdot h^2 A^{-1} \left(q_2^n - q_2^{t-1} - \frac{k_d^2}{2} (\psi_1^{t-1} - \psi_1^{t-2}) \right) \right] dt + 0.1 \sqrt{dt} \mathcal{N}(0, 1) \quad (43)$$

$$= [a_0 + a_1 Y] dt + b_2(X, t) dW_2(t), \quad (44)$$

$$A_0 = \left[\frac{1}{dt} \cdot h^2 A^{-1} \left(q_1^{n+1} - q_1^n + \frac{k_d^2}{2} \psi_2^{t-1} \right) \right], \quad A_1 = \frac{1}{dt} \cdot -\frac{h^2 k_d^2}{2} A^{-1}, \quad (45)$$

$$a_0 = \left[\frac{1}{dt} \cdot h^2 A^{-1} \left(q_2^n - q_2^{t-1} - \frac{k_d^2}{2} (\psi_1^{t-1} - \psi_1^{t-2}) \right) \right], \quad a_1 = 0. \quad (46)$$

It should be noted that the ψ_2 terms that are computed at previous timesteps are independent of ψ_2^n , because they are already known. This allows the previously predicted values to be a part of observation, which leads a_1 to be a zero matrix. This interestingly depicts that the recovery of posterior mean is completely independent of the observations of ψ_2 itself, which equates to the full dependence of other variables. Such property corroborates the strong coupling between state variables, fulfilling the motivation to alter the native approach. The pseudo code for this algorithm is provided below.

Algorithm 3 Two-layer QG CGNS advanced solver

Require: {All the parameters in Tables 2 and 3}
init constants, time variables and mesh constraints
init compute the invariant matrix A before time marching
init ψ^1, q^1 and μ_f for both layers given the initial ψ
for $t = 1 : \frac{N_t}{100} - 1$ **do**
 compute q^{n+1} by solving Equation (3) with (9)
 compute ψ^{n+1} by solving Equation (4) with (12)
 update $\Sigma\psi$ and Σq for R_f
end for
init R_f based on $\psi^{1:\frac{N_t}{100}}, \Sigma\psi, q^{1:\frac{N_t}{100}}$ and Σq
for $t = \frac{N_t}{100} : N_t$ **do**
 compute observational noise
 compute ψ_2^{n+1} with μ_f^n
 compute q_1^{n+1} and q_2^{n+1} based on ψ^{n+1}
 find A_0, A_1, a_0 and a_1 with Equations (26) and (27)
 compute μ_f^{n+1} via CGNS framework with Equation (45)
 compute R_f^{n+1} via CGNS framework with Equation (46)
end for
return $\psi_2^{1:N_t}$ and $\mu_f^{1:N_t}$

4 Numerical experiments

In this section, we study three numerical simulation scenarios for each initial streamline function (sinusoidal and Gaussian in Table 2). Firstly, the CGNS framework that observes both layers of the QG model in Section 3.2 was simulated along with the numerical solution in Section 2 by following Algorithms 2 and 1,

respectively. Similarly, the DA for recovering the second layer given only the first layer was simulated with Algorithm 3. Finally, we consider a simplified scenario where sea ice floe dynamics were coupled with the ocean flow modeled by the two-layer QG model. The processor that ran the simulation was Intel i3-8130U CPU with 8GB RAM. This low computational demand is in line with recent QG DA study regarding efficient and low-cost implementations [31]. All the artifacts, including the MATLAB code, simulation videos, and performance evaluation, can be found on the [Github repository](#) [35].

4.1 EuDA for recovery of the vorticity and the second-layer flow

Figures 2, 3, 4 and 5 illustrate the simulations of Algorithms 2 and 3 compared with Algorithm 1, respectively. Qualitatively speaking, both recoveries visually seem to be indistinguishable from their true values across the two streamline functions. Nevertheless, the explicit visualization of the difference between the recovery and the truth reveals further insights for each recovery. For the recovery of the vorticity, the magnitude of difference tends to follow that of the recovered attribute. For example, Figure 3 indicates the difference is most notable in the center, where the main flow is present. This trend does not hold for the recovery of the second-layer flow. It can be seen that the difference mostly resembles a noise, suggesting Algorithm 3 can achieve faithful recovery regardless of the magnitude of variables unlike Algorithm 2.

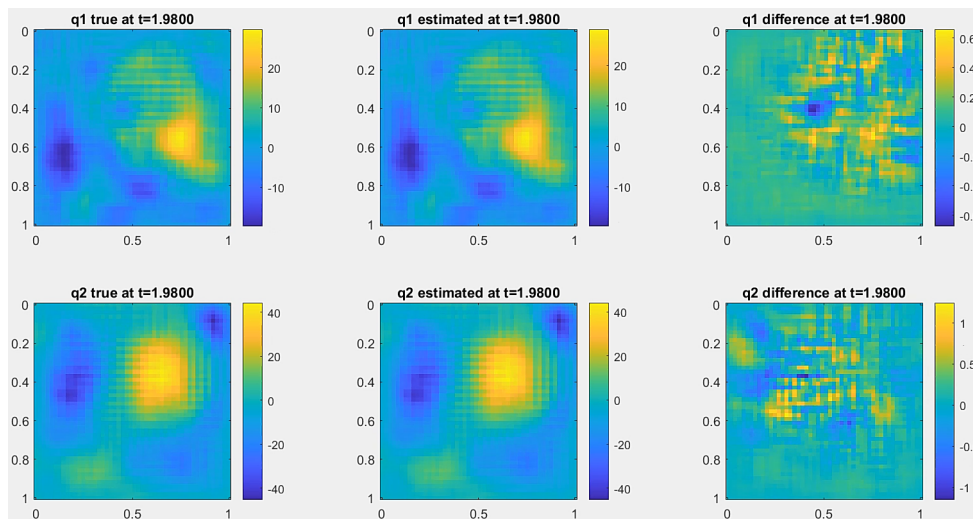


Figure 2: Simulation of true and recovered q at $t = 1.98$ with sinusoidal streamline function

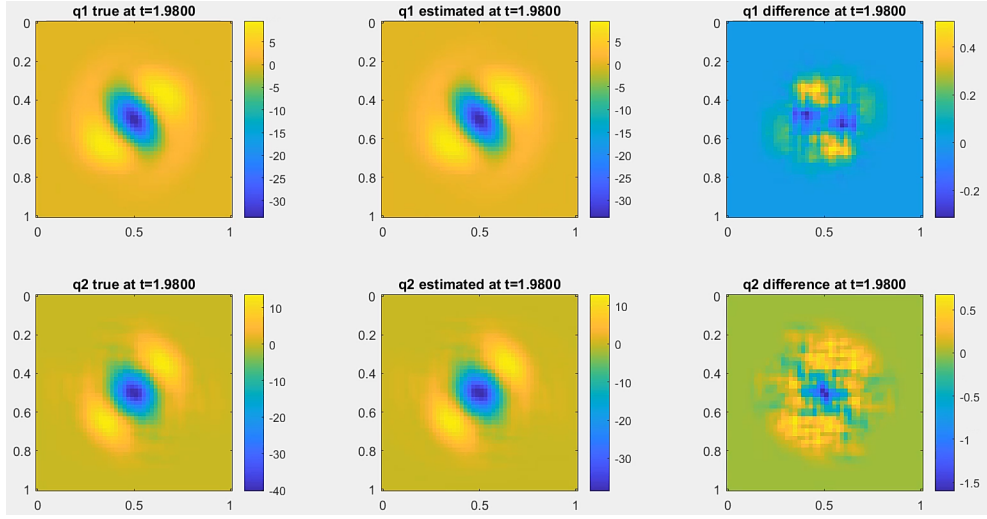


Figure 3: Simulation of true and recovered q at $t = 1.98$ with Gaussian streamline function

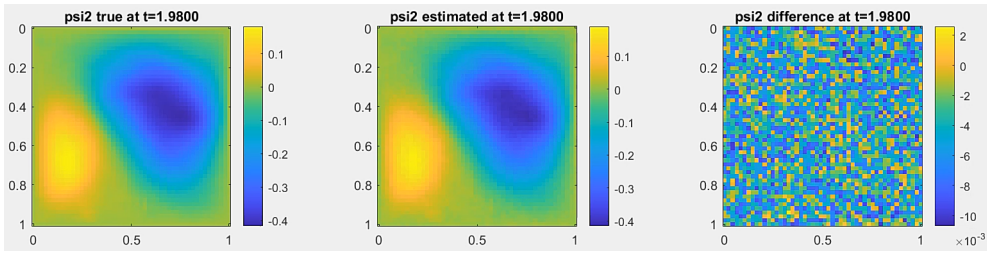


Figure 4: Simulation of true and recovered ψ_2 at $t = 1.98$ with sinusoidal streamline function

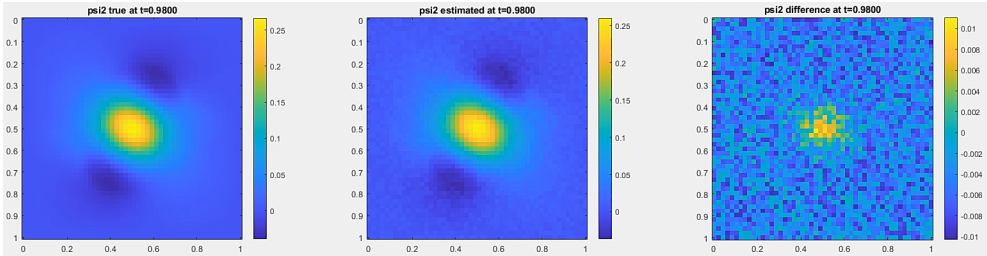


Figure 5: Simulation of true and recovered ψ_2 at $t = 0.98$ with Gaussian streamline function

To quantitatively evaluate the performance of the main algorithm (3), Root mean squared error (RMSE) and pattern correlation (Corr) were used as two path-wise metrics [34] across different dimensions of the mesh ($\{10 \times 10, 30 \times 30, 50 \times 50\}$) and timesteps ($\{500, 1000, 3000, 5000, 10000, 15000, 20000\}$). Both metrics are the most common ways to compare the posterior mean and truth. RMSE indicates the average deviation between the simulated state and the true state. Meanwhile, Corr highlights how well the spatial pattern of the simulation aligns with the reference model. They are defined as follows. Let μ and x be vectors for the posterior mean and truth of a recovered variable of each cell, respectively, with n being the total number of

cells. Then,

$$\mathbf{RMSE} = \left(\sqrt{\frac{\sum_{i=1}^P (\mu_i - x_i)^2}{n}} \right) / \mathbf{std}(x), \text{ and} \quad (47)$$

$$\mathbf{Corr} = \frac{\sum_{i=1}^P ((\mu_i - \mathbf{mean}(\mu))(x_i - \mathbf{mean}(x)))}{\sqrt{\sum_{i=1}^P (\mu_i - \mathbf{mean}(\mu))^2} \sqrt{\sum_{i=1}^P (x_i - \mathbf{mean}(x))^2}}. \quad (48)$$

The RMSE is always non-negative, with lower RMSE values indicating a more accurate posterior mean estimate. Since the RMSE in Equation (47) is normalized by the standard deviation of the true data, an RMSE above 1 implies that the error in the posterior mean estimate exceeds the mean variation in the true data [34]. Pattern correlation ranges from -1 to 1, where larger absolute values denote greater similarity between the two profiles [34]. Typically, a reliable estimate achieves a pattern correlation above 0.5.

Figure 6 illustrates the results of RMSE, Corr, and computation time as plots. The normalized computation time refers to actual computation time divided by $N_t \times N_x^2$ to depict the time complexity of the algorithm, which is often hard to capture in the original time plot, especially with only three coordinates for each line. Therefore, the linearity in the normalized graph apart from $N_t = 500$ indicates the time complexity of $O(N_t \times N_x^2)$, which follows from an $N_x \times N_y$ (where $N_x = N_y$) matrix performing operations iteratively over N_t times. This can be further corroborated by comparing the raw computation time across different N_t when N_x is fixed to 50. For example, $N_t = 5000$ and $N_t = 10000$ in such settings lasted about 400 and 800 seconds, respectively, which is proportional to the ratio between the N_t s. Similarly, $N_t = 20000$ indeed ran for 1800 seconds, which is roughly quadruple and double of the other two settings, respectively. Furthermore, it can be seen that the most involved simulation approximately took 30 minutes under the below-average computational resources, suggesting a low demand for such operations.

Meanwhile, the RMSE metric, plotted on a logarithmic x-axis, effectively captures the algorithm's performance across timesteps N_t and grid sizes N_x . Notably, RMSE values decrease steadily as N_t increases, showing that the error between the posterior mean estimate and the true state reduces over time. This decline in RMSE appears to converge toward a value around 0.1, irrespective of the grid size. This convergence suggests that the DA algorithm achieves a consistent level of accuracy over time, largely independent of spatial resolution. In other words, as the time marching scheme progresses, the DA framework consistently refines its estimates, reinforcing its robustness across varying spatial scales. This outcome highlights one of DA's primary strengths: its adaptability and effectiveness in multiscale settings, where it can achieve reliable accuracy regardless of spatial granularity. The Corr metric exhibits a general upward trend with respect to the number of timesteps across different grid sizes, indicating improved alignment between the model estimate and the true state as the assimilation process advances. However, the influence of N_x on Corr is significant. Larger grid sizes consistently yield higher Corr values, showing that higher spatial resolution enables the algorithm to better capture the pattern of the true state. For example, Corr is maximized at 0.92 for $N_x = 50$, while $N_x = 10$ can go as high as 0.64. Interestingly, Corr values show diminishing returns after $N_t = 3000$, where further increases in N_t contribute less to improving Corr across all N_x . This observation suggests that while finer temporal resolution continues to provide marginal benefits, the spatial resolution ultimately becomes a limiting factor in the Corr metric's growth. This outcome implies the necessity of sufficiently high grid resolution N_x for more detailed alignment with the true state pattern.

Overall, the evaluation indicates the EuDA of the two-layer QG model via CGNS performed well with

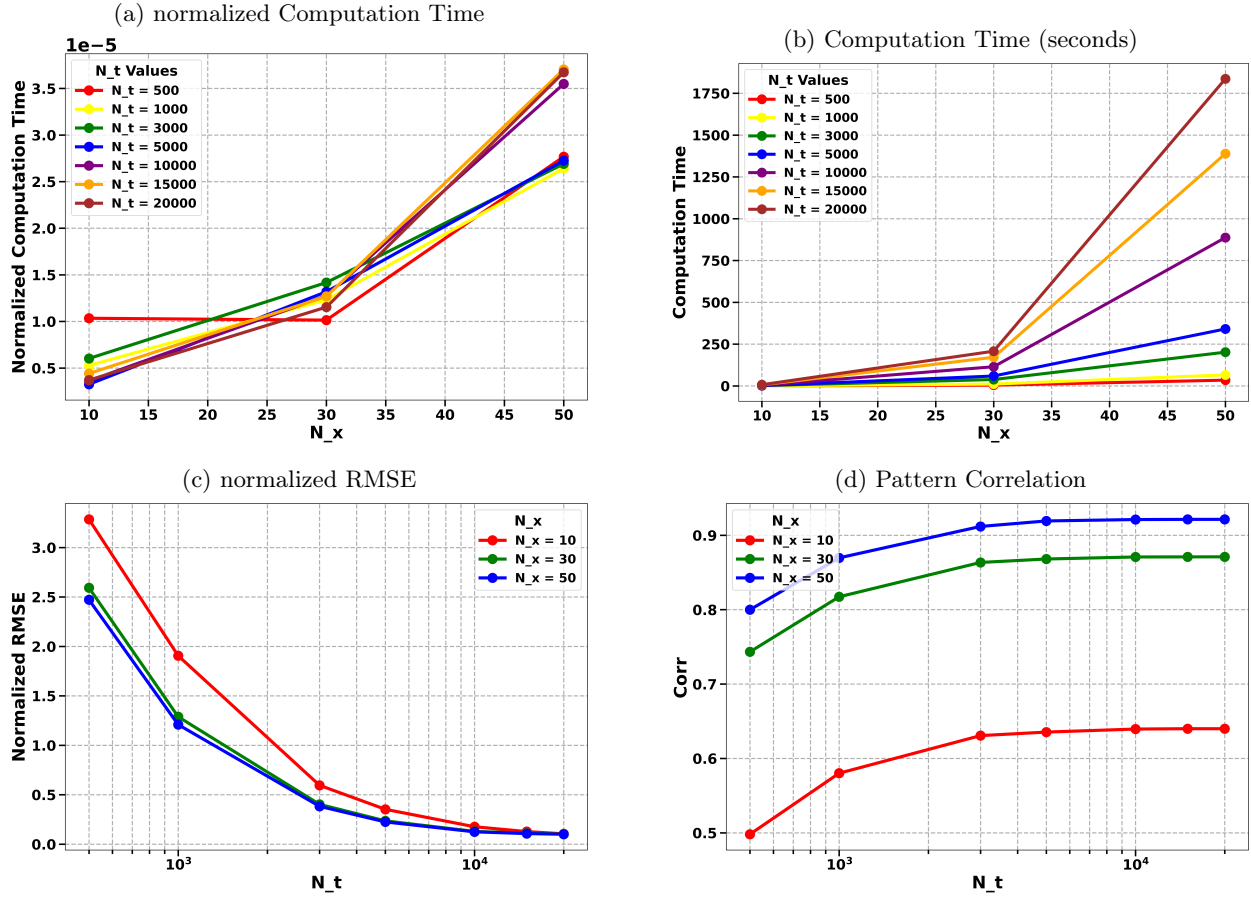


Figure 6: Performance evaluation of two-layer QG model simulation via CGNS

decreasing RMSE and increasing Corr when refining the grids.

4.2 An application to sea ice floe dynamics with QG ocean flow

We assume no floe collision and the floe particles are dragged by the ocean flow in the upper ocean layer. The recovered attributes were used to interpolate the trajectories of particles with the simplified Lagrangian particle model (49) and (50), coupled with Equation (51):

$$\frac{d\mathbf{x}_1}{dt} = \mathbf{v}_1 + \sigma_x \dot{\mathbf{W}}_1, \quad (49)$$

$$\frac{d\mathbf{v}_1}{dt} = \beta(\mathbf{u} - \mathbf{v}_1), \quad (50)$$

$$\mathbf{u}_i = \left(\frac{-d\psi_i}{dy}, \frac{d\psi_i}{dx} \right), \quad (51)$$

where β is the ocean drag coefficient. $\beta = 0.1$ was chosen by default for numerical simulations.

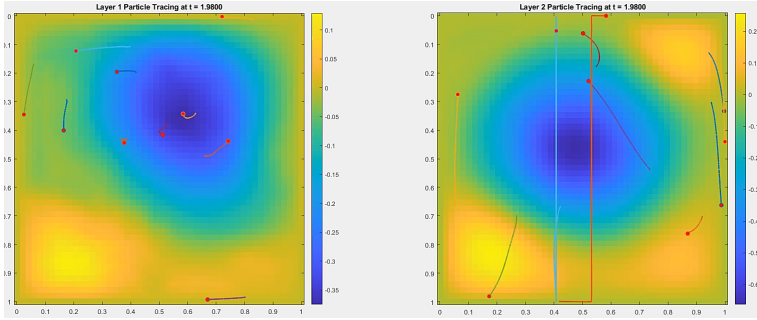


Figure 7: Simulation of particle tracing of two-layer QG model at $t = 1.98$ with sinusoidal streamline function

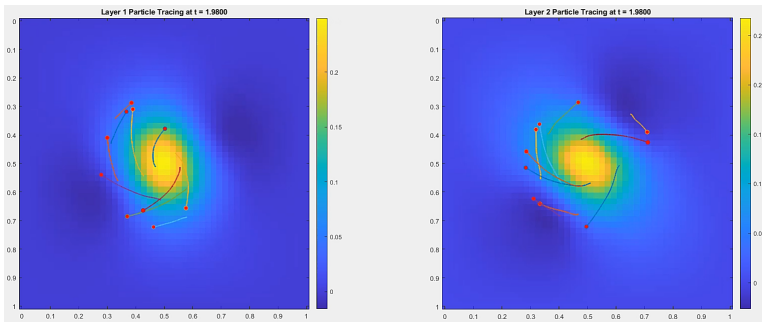


Figure 8: Simulation of particle tracing of two-layer QG model at $t = 1.98$ with Gaussian streamline function

Figures 7 and 8 show a few snapshots of the simulation. Note that the jump (discontinuity in the trajectories) of particles in Figures 7 and 8 is a result of the doubly periodic boundary condition fully trapping all particles inside the grid. It is also worth noting that the sparsity of recovery via Algorithm 3 is much higher than that of Algorithm 2. This experiment example demonstrates the potential application of EuDA in the physical domain to sea ice floe dynamics, in contrast to DA algorithms, which rely on a large number of Fourier modes for accuracy in capturing features in the physical domain.

5 Conclusion

This study developed an EuDA framework by integrating CGNS for a two-layer QG model in the physical domain. The results demonstrate that this framework maintains low RMSE values across time and grid resolutions while achieving strong spatial alignment with the true state. The pattern correlation analysis highlights the framework’s capacity to adapt across multiple scales, revealing that further improvements can be made when using a finer grid. These findings collectively affirm the robustness and scalability of the proposed EuDA formulation, providing a foundation for more advanced data assimilation strategies in physical domains.

Building on these outcomes, several promising directions for future work are as follows. Firstly, one may leverage neural networks (NN) on a cell-by-cell basis, which represents a key pathway toward parallelizing the computational processes inherent in the proposed framework. This approach could allow efficient parallelization that maximizes computational efficiency [26]. Another intriguing extension involves exploring

whether the fundamental state variables can be accurately recovered solely by coupling the QG model with sea ice particle dynamics, with observation of the particle displacements. Current methods primarily rely on direct observations of ψ and q , but a system where only particle trajectories are observed could offer a more feasible setup in real-world applications. This approach would require developing advanced techniques, such as the recently developed Lagrangian-Eulerian multiscale DA (LEMDA) [11], to reconstruct field states from sparse data in the physical domain.

Furthermore, it is essential to establish rigorous analytical conditions for the convergence of the two-layer QG CGNS solver, ensuring stability across various parameter settings. Such conditions would enable precise control over model parameters and provide clear boundaries within which the solver maintains both accuracy and stability. It would serve as a critical tool for designing and fine-tuning the DA process, allowing researchers to optimize computational resources without compromising the fidelity of the posterior mean estimate [20]. Extending the two-layer QG model to support more layers would offer the potential for modeling complex systems that may involve more extreme vertical stratification, such as those found in oceanographic and atmospheric flows [27, 6]. Each additional layer would introduce unique challenges related to inter-layer coupling and the propagation of uncertainties through the model, thus requiring a refined DA framework. In this respect, the proposed two-layer framework can serve as an inductive step for a scalable approach, incrementally increasing model complexity.

In conclusion, this work has laid a solid foundation for advancing data assimilation in the physical domain by demonstrating a stable and multiscale EuDA framework based on CGNS. The proposed approach provides a coherent and computationally efficient pathway for assimilating nonlinear, high-dimensional systems, paving the way for more accurate and interpretable physical-domain modeling.

Acknowledgements

Q.D. is partially supported by start-up funding from the Yau Mathematical Sciences Center, Tsinghua University, the Australian National Computing Infrastructure (NCI) national facility under grant zv32, and the HMI Computing for Social Good Seed Research Grant.

References

- [1] Peter Bauer, Alan Thorpe, and Gilbert Brunet. The quiet revolution of numerical weather prediction. *Nature*, 525(7567):47–55, 2015.
- [2] Jule G. Charney. The Dynamics of Long Waves in a Baroclinic Westerly Current. *Journal of Meteorology*, 4(5):136–162, 1947.
- [3] Jean-Paul Chehab and Maithem Trabelsi Moalla. Numerical simulations of a 2D quasi geostrophic equation, 2010.
- [4] Nan Chen, Yingda Li, and Honghu Liu. Conditional Gaussian Nonlinear System: A Fast Preconditioner and a Cheap Surrogate Model for Complex Nonlinear Systems. *Chaos: An Interdisciplinary Journal of Nonlinear Science*, 32(5):053122, May 2022. Part of the Focus Issue on Theory-informed and Data-driven Approaches to Advance Climate Sciences.

- [5] Nan Chen and Andrew J Majda. Conditional Gaussian systems for multiscale nonlinear stochastic systems: Prediction, state estimation and uncertainty quantification. *Entropy*, 20(7):509, 2018.
- [6] Colin Cotter, Dan Crisan, Darryl Holm, Wei Pan, and Igor Shevchenko. Data Assimilation for a Quasi-Geostrophic Model with Circulation-Preserving Stochastic Transport Noise. *Journal of Statistical Physics*, 179(5):1186–1221, 2020.
- [7] J Austin Cottrell, Thomas JR Hughes, and Yuri Bazilevs. *Isogeometric analysis: toward integration of CAD and FEA*. John Wiley & Sons, 2009.
- [8] Richard Courant, Kurt Friedrichs, and Hans Lewy. Über die partiellen Differenzgleichungen der mathematischen Physik. *Mathematische Annalen*, 100(1):32–74, 1928.
- [9] H.C. Davies and H. Wernli. Quasi-geostrophic theory. In James R. Holton, editor, *Encyclopedia of Atmospheric Sciences*, pages 1787–1794. Academic Press, Oxford, 2003.
- [10] Quanling Deng, Pouria Behnoudfar, and Victor M Calo. SoftIGA: Soft isogeometric analysis. *Computer Methods in Applied Mechanics and Engineering*, 403:115705, 2023.
- [11] Quanling Deng, Nan Chen, Samuel Stechmann, and Jihua Hu. LEMDA: A Lagrangian-Eulerian Multiscale Data Assimilation Framework, 2024.
- [12] Quanling Deng and Alexandre Ern. SoftFEM: revisiting the spectral finite element approximation of second-order elliptic operators. *Computers & Mathematics with Applications*, 101:119–133, 2021.
- [13] Alexandre Ern and Jean-Luc Guermond. *Theory and practice of finite elements*, volume 159. Springer, 2004.
- [14] Geir Evensen. Sequential data assimilation with a nonlinear quasi-geostrophic model using Monte Carlo methods to forecast error statistics. *Journal of Geophysical Research: Oceans*, 99(C5):10143–10162, 1994.
- [15] Geir Evensen. *Data Assimilation: The Ensemble Kalman Filter*. Springer Science & Business Media, 2009.
- [16] Eugenia Kalnay and Shu-Chih Yang. Accelerating the spin-up of Ensemble Kalman Filtering. *Quarterly Journal of the Royal Meteorological Society*, 136(651):1644–1651, 2010.
- [17] Heiner Kornich, S Wahl, and S Basu. Dynamic downscaling of atmospheric fields for mesoscales and sub-mesoscales. *Journal of Geophysical Research: Atmospheres*, 113:D07108, 2008.
- [18] Nathan Kutz. *Data-Driven Modeling & Scientific Computation*. Oxford University Press, 2013.
- [19] Kody Law, Andrew Stuart, and Konstantinos Zygalakis. *Data Assimilation: A Mathematical Introduction*. Springer, 2015.
- [20] Andrew J Majda and John Harlim. A new perspective on multiscale geophysical data assimilation. *SIAM Review*, 54(2):377–418, 2012.

- [21] Andrew J. Majda, John Harlim, and Boris Gershgorin. Mathematical strategies for filtering turbulent dynamical systems. *Discrete and Continuous Dynamical Systems - Series A*, 27(2):441–486, 2010.
- [22] HT. Tachim Medjo. Numerical Simulations of a Two-Layer Quasi-Geostrophic Equation of the Ocean. In *SIAM Journal on Numerical Analysis*, 2000, vol 37, pages 2005–2022. Society for Industrial and Applied Mathematics, 2000.
- [23] Chen Nan. *Stochastic Methods for Modeling and Predicting Complex Dynamical Systems*. Springer, 2023.
- [24] Eiichi Oka. *Nonlinear Solutions to a Two-Layer Quasi-Geostrophic Model of the Gulf Stream*. PhD thesis, Old Dominion University, Shimizu, Japan, December 1989.
- [25] Bernt Oksendal. *Stochastic Differential Equations: An Introduction with Applications*. Springer, 6 edition, 2010.
- [26] Jaideep Pathak, Zhixin Lu, Brian Hunt, Michelle Girvan, and Edward Ott. Using machine learning to augment coarse-grid computational fluid dynamics simulations. *Journal of Computational Physics*, 375:973–991, 2018.
- [27] Joseph Pedlosky. *Geophysical Fluid Dynamics*. Springer Science & Business Media, 1987.
- [28] S. G. Penny, E. Bach, K. Bhargava, C.-C. Chang, C. Da, L. Sun, and T. Yoshida. Strongly Coupled Data Assimilation in Multiscale Media: Experiments Using a Quasi-Geostrophic Coupled Model. *Journal of Advances in Modeling Earth Systems*, 11(6):1803–1829, 2019.
- [29] Di Qi and Andrew J Majda. Low-dimensional reduced-order models for statistical response and uncertainty quantification: Two-layer baroclinic turbulence. *Journal of the Atmospheric Sciences*, 73(12):4609–4639, 2016.
- [30] Michael Roth, Gustaf Hendeby, Carsten Fritsche, and Fredrik Gustafsson. The Ensemble Kalman filter: a signal processing perspective. *EURASIP Journal on Advances in Signal Processing*, 2017.
- [31] François Rozet and Gilles Louppe. Score-based Data Assimilation for a Two-Layer Quasi-Geostrophic Model, 2023.
- [32] Geoffrey K. Vallis. *Atmospheric and Oceanic Fluid Dynamics*. Second Edition. Cambridge University Press, 2017.
- [33] Zhongrui Wang, Nan Chen, and Di Qi. A Nonlinear Data Assimilation Algorithm with Closed-Form Approximations for Multi-Layer Flow Fields. *Monthly Weather Review*, 2025.
- [34] Daniel S. Wilks. *Statistical Methods in the Atmospheric Sciences*. Academic Press, 3rd edition, 2011.
- [35] Geun Yun. Quasi_geostrophic_model_for_lemda. https://github.com/geun-yun/Quasi_geostrophic_model_for_LEMDA/tree/main, 2024.